16th International Conference on Greenhouse Gas Control Technologies, GHGT-16

23rd -27th October 2022, Lyon, France

Precipitation-Induced Geometry Evolution in Porous Media: Numerical and Experimental Insights based on New Model on Probabilistic Nucleation and Mineral Growth

Mohammad Nooraiepour[a,*], Mohammad Masoudi[a], Nima Shokri[b] and Helge Hellevang[a]

[a] *CO_2 Storage Research Group, Department of Geosciences, University of Oslo, P.O. Box 1047 Blindern, 0316 Oslo, Norway*
[b] *Institute of Geo-Hydroinformatics, Hamburg University of Technology, Am Schwarzenberg-Campus 3 (E), 21073 Hamburg, Germany*

Abstract

Precipitation and growth of solid phases during a reactive fluid flow and solute transport are critical in many natural and industrial systems. Mineral nucleation and growth is a prime example where (geo)chemical reactions give rise to geometry evolution in porous media. The precipitation reactions can reduce the amount of void space, alter pore space connectivity and morphology, modify tortuosity, deteriorate permeability, and change the fluid flow and solute transport. Additionally, precipitation events reshape the available surface area for growth, leading to changes in reactivity, reaction progress, and reaction rates. The target is to ideally limit the mineral growth in many applications, such as avoiding damage to reservoir permeability due to solid precipitation near CO_2 injection wells. In other cases, maximizing mineral growth in porous media can be highly favorable, such as sealing fractured caprocks or increasing mineral trapping in the sequestration sites. Understanding, controlling, and predicting this reactive transport phenomenon is challenging because it requires coupling flow, transport, and chemical processes often characterized by different temporal and spatial resolutions. Nucleation is the pre-growth process that controls the primary position of any mineral precipitation and subsequent growth dynamics. Mineral nucleation is a probabilistic process where crystals might nucleate anywhere given similar conditions, such as surface properties, supersaturation, and temperature. It is imperative to use a probabilistic approach or an upscaled physically sound representation to understand the effect of mineral precipitation on porous medium hydrodynamics. Motivated by the importance of incorporating stochastic dynamics of nucleation and growth kinetics in studying various multiphase and multiscale processes occurring in geo-environmental and geo-energy systems, this paper provides numerical and experimental insights into the recently proposed probabilistic nucleation model. We present laboratory experiments (microfluidic and flow-through column reactor) and pore-scale reactive Lattice Boltzmann Method (LBM) numerical simulations. As variations in the properties of the porous medium are intimately linked to the spatial distribution of the precipitation events, we quantify the evolution of experimental and numerical modeled systems at different physiochemical conditions by mapping the disorder of the system (Shannon's entropy) induced by the spatial mineral distributions across time. We use experimental and numerical results to show the importance of the spatial and temporal location and distribution of nucleation and growth events, particularly when the interplay among several determining parameters is inevitable. The results show that probabilistic nucleation contributes to broad stochastic distributions in both amounts and locations of crystals in temporal and spatial domains.

Keywords: Nucleation; Precipitation; Crystal Growth; Porous Media; Reactive Transport; Fluid Flow; Entropy; LBM.

* Corresponding author. *E-mail address:* mohammad.nooraiepour@geo.uio.no

1. Introduction

Interface-coupled precipitation and dissolution (geo)chemical reactions play an important role in studying coupled thermo-hydro-mechanical-chemical (THMC) phenomena and processes in the subsurface environment [1–5]. Subsurface reactive fluid flow and solute transport is central to several pressing energy, environment, and societal challenges, including the geological storage of carbon dioxide (CO_2). Mineral nucleation and growth is a prime example of interface-coupled dissolution and precipitation (ICDP) reactions giving rise to geometry evolution in porous media [1,6–11]. When precipitation reactions are ample, crystal accumulations can dramatically reduce porosity (amount of void space) [8,10,12]. Alteration in pore volume, in turn, changes the connectivity of the pore space [13,14]. Alterations in porosity and connectivity lead to pore space morphology changes, affecting properties such as tortuosity and permeability of the altered medium and, as a result, changes in fluid flow and solute transport [15–19]. Additionally, precipitation reshapes the available surface area for growth, leading to changes in the system's reactivity, reaction progress, and rates [1,12,20–22]. Therefore, understanding and predicting parameters and mechanisms governing ICDP is critical for studying (geo)chemical fluid-rock interactions (THMC) and the effects on geoenergy and geoenvironmental systems across spatiotemporal scales.

Understanding the consequences of mineral nucleation and growth within the porous medium and the fate of fluid flow and solute transport requires spatial and temporal knowledge of the location and amount of solid precipitation. The reactive transport models (RTMs) only then can provide precise and realistic predictions on the intricate interplay between transport mechanisms and reaction kinetics and, therefore, advection-diffusion-reaction (ADR). However, accurately representing the dynamics and dimensionality of mineral nucleation and growth (or, in general, ICDP) in porous media is still challenging [8,9,12,13,23–26]. The RTM complexity arises from the ADR dependence on multiple parameters, including fluid flow, fluid chemistry, and the mineral substrate that might vary notably over different time- and length-scales [3,9,27–32]. Prediction of these complex perturbations requires RTMs that are often far from trivial because of the dynamic interplay of the several parameters in action simultaneously. Knowledge of the individual mineral reactivity, representative mathematical equations for the thermodynamics and mineral kinetics, and numerical models are needed to solve the strongly non-linear systems of coupled advection-diffusion-reaction at spatiotemporal scales ranging from individual pore network to entire geological basins [12,13,33,34].

For the first time, we recently proposed a probabilistic nucleation and growth model [8,12], underscoring the importance of incorporating stochastic nucleation in space and time before crystal formation. Nucleation events, which are probabilistic [8,12,28,35–37], occur only after a specific induction time and when species concentrations reach a certain threshold. A crystal nucleus forms from a supersaturated aqueous solution during a nucleation event. Then it undergoes stabilization, growth, ripening, phase transformation, and crystallization [38]. The nucleus may form in the bulk of a fluid called homogeneous nucleation or form at the solid-liquid interface called heterogeneous nucleation. The probabilistic nucleation model has been adopted for studying CO_2-induced clogging in porous media [10] and the impact of heterogeneous substrate properties [22], for investigating ICDP with a micro-continuum approach [1], for pore-scale modeling of crystal nucleation and growth [39,40]. The new probabilistic nucleation and growth model may receive experimental inputs describing the relationship between experimental/deterministic induction time (τ_N) and the probabilistic induction time (τ_P) for constructing process-specific probability distribution functions of forming a nucleus [12]. As a Supplementary Information in Nooraiepour et al. [12], the Python script handling pore-scale probabilistic nucleation model was provided for open-access usage to assist researchers studying reactive transport processes in the straightforward implementation of the code into the RTM simulations.

As presented in Figure 1, we suggest that reactive transport processes can be better studied by introducing probabilistic and deterministic domains time- and length-scales (system physical size). Figure 1 shows the conceptual framework we propose to handle and predict mineral nucleation and growth for various spatiotemporal resolutions, where the horizontal axis represents system temporal size (time-scale), and the vertical axis indicates system spatial size (length-scale). The vertical axis can also proxy the available surface area for the ICDP occurrence. The proposed framework consists of two domains, namely, probabilistic and deterministic domains. A reactive system may exhibit a continuous behavior from entirely probabilistic to nearly deterministic.

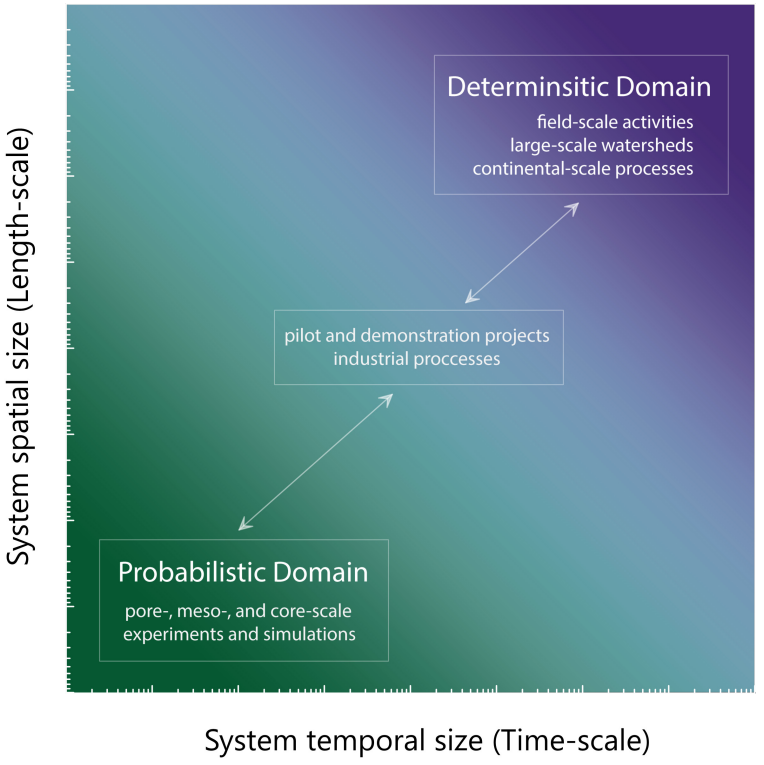

Fig. 1. Conceptual framework specifying probabilistic and deterministic domains for predicting mineral nucleation and growth across spatiotemporal scales. The induction time determines the boundary between the probabilistic and deterministic domains.

Pore-scale, meso-scale and core-scale experimental and numerical studies fall into the probabilistic domain (Fig. 1). Field-scale activities, catchment scale, and continental-scale are placed in the deterministic domain. Processes and systems that share characteristics of both domains are placed in the transitory realm. Pilot projects and most industrial processes are two examples of the transitory realm. To ensure that simulations in larger scales incorporate the underlying physics behind a particular phenomenon, the results of any simulations (or experiments) in the probabilistic domain should be upscaled to the larger domains. Porosity-permeability relations used in continuum scale modeling to account for precipitation/dissolution are examples of this upscaling between two domains. However, none of the available porosity-permeability relationships have taken into account the probabilistic dynamics and dimensionality [10].

The time interval is entirely different for different reactions and different physiochemical conditions. The interface between the two domains is controlled by induction time and is a function of temperature, supersaturation, interfacial free energy, etc. As induction time for a given process changes, it moves the boundary between the domains and determines how fast or slow it will enter the deterministic domain. For extended times and large volumes, the continuum variable in the deterministic domain undergoes slight changes considering spatiotemporal size, particularly when system properties are averaged and simplified in macroscopically homogeneous continuum-scale investigations. However, in the probabilistic domain below a specific time span and volume, marked variations are expected.

We present laboratory experiments (flow-through column reactor and microfluidic devices) and pore-scale reactive Lattice Boltzmann Method (LBM) numerical simulations. As variations in the properties of the porous medium are intimately linked to the spatial distribution of the precipitation events, we quantify the evolution of experimental and numerical modeled systems at different physiochemical conditions by mapping the disorder of the system (Shannon's entropy) induced by the spatial mineral distributions across time. We use experimental and numerical results to show the importance of the spatial and temporal location and distribution of nucleation and growth events when the interplay among several determining parameters is inevitable. The results show that probabilistic nucleation contributes to broad stochastic distributions in both amounts and locations of crystals in temporal and spatial domains.

2. Materials and Methods

2.1. Flow-through column reactor experiment

Flow-through column experiment was performed using a custom-designed glass tube reactor (40 cm in length and 14 mm in inner diameter). As shown in Figure 2a, the experimental column was packed with crushed calcium carbonate aggregates (first 4 cm) and basaltic glass (the rest 36 cm). Calcium carbonate aggregates provided the necessary solute concentration (Ca^{2+}) in contact with the injected CO_2-acidified seawater. The basaltic glass of tholeiitic composition (fine-grained extrusive igneous rock, which is relatively rich in silica and poor in sodium) from Stapafell (Reykjanes Peninsula, Iceland) [41] was used as a mineral nucleation substrate for this reactive transport experiment. Basaltic glass offers fast reactivity compared to crystalline materials [41,42], provides an adequately homogenous chemical composition as the substrate surface, and the dark color makes the identification of secondary carbonate phases straightforward.

For experimental fluid preparation, we first sampled approximately 1 liter of seawater from the Oslo Fjord and filtered the fluid through a 0.45 µm Millipore© filter. In the Oslo Fjord, the seawater is only slightly affected by the inflow of freshwater mixing but shows a close chemical compositional to average North Sea seawater. A CO_2 bottle (grade 5.2, scientific carbon dioxide, Praxair Norge) was used to prepare CO_2-charged seawater at 4 MPa gaseous CO_2 pressure within a pressurized fluid accumulator (transfer vessel) inside a forced convection benchtop oven (Despatch LBB series). During the experiment, CO_2-reach natural brine was injected at a rate-controlled regime using a dual-piston ISCO pump from the bottom port. A steady flow of CO_2-charged seawater of 0.005 ml/min (approximately 20 cm/day) was then achieved. Fluid sampling was performed at the column inlet at discrete times (3 days intervals) and continuously at the column outlet. The acidity of aqueous solutions was analyzed immediately after sampling using a standard benchtop pH meter. The experiments were carried out at 80°C with atmospheric CO_2 pressure at the outlet for 30 days. A detailed description of the experimental setup was given in [7,28,43,44].

2.2. Batch-type microfluidic experiment

A natural heterogeneous (multi-mineral) sandstone (Brumunddal sandstone deposited north of the Oslo Rift) was selected as a geomaterial substrate (disk shape specimens of 1.5 cm height and 2.5 cm diameter). For the calcium carbonate synthesis, we prepared stock solutions from respective crystalline solids (ACS re-agent, ≥ 99.8%) of calcium chloride ($CaCl_2$) and sodium bicarbonate ($NaHCO_3$) by adding the well-defined weight of salts to the DI-water (Milli-Q water). We used the PHREEQC v3 package [45] for aqueous geochemical calculations to compute solute supersaturation before the experiments. The supersaturation (Ω) is defined as the saturation ratio given by the ion activity product divided by the equilibrium constant. The stoichiometry estimates were based on equilibrium with atmospheric CO_2 pressure. Nine sets of experiments were conducted at three supersaturations (Ω = 15, 50, and 130x) and three temperatures (T = 20, 40, and 60°C). For each Ω, experiments at three different temperatures were performed. The elapsed time (t) for the tests were 6, 48, and 96 hours. Therefore, a total of 27 experiments (3×3×3 sets of Ω-T-t) were carried out. Further details of the laboratory procedure were given in [9].

2.3. Solid surface characterization

Scanning electron microscopy (SEM) via backscattered (BSE) and secondary electrons (SE) imaging was used to study the surface structure and mineral growth. The energy-dispersive x-ray spectroscopy (EDS) was used for chemical analyses and element mapping. Three random locations were selected and analyzed for SEM-EDS surface mapping for each substrate. A mosaic map of nine SEM-EDS images covering an approximately 10.5 mm^2 area was acquired with a spatial resolution of 1 µm. A variable pressure Hitachi SU5000 FE-SEM (Schottky FEG) equipped with a Dual Bruker XFlash system and a high-resolution automated electron backscatter diffraction (HR EBDS) was used to perform the SEM imaging and EDS spectroscopy. Carbon coating of substrates was carried out using a Cressington Carbon Coater to improve image quality, increase chemical analysis precision, and better topographic examination while avoiding surface charging and potential thermal damages.

For digital image processing, the superimposed calcium phase map (color-coded in green) on the surface mosaic map was selected as an input (e.g., Fig. 4a). A semi-automated workflow for digital image processing of surface mosaic maps was defined to identify and quantify precipitated crystals. First, two-dimensional surface maps were filtered with a non-local means filter to remove noise and improve demarcation between phases. Subsequently, contrast enhancement filters were applied (histogram equalization and linear contrast adjustment). The mosaic maps were segmented and converted into binary images based on the histogram of grey values (two distinct distributions). The inverted (mask) transformation of the binary map was analyzed in the ImageJ/Fiji [46] to identify, outline, and quantify the precipitated calcium carbonate crystals.

2.4. Lattice Boltzmann Method (LBM) numerical simulation

For numerical simulation of surface mineral growth, we used the Lattice Boltzmann (LB) model to solve the advection-diffusion-reaction (ADR) equations for tracking the concentration of different species. We developed a reactive transport model based on our recently proposed probabilistic nucleation and crystal growth theory [12]. In the newly proposed probabilistic nucleation theory, the probabilistic induction time (τ_P) is considered a random variable statistically distributed around the deterministic mean induction time (τ_N). The deterministic mean induction time (τ_N) can be obtained by laboratory experiments or approximated by the classical exponential nucleation rate equation suggested in the classical nucleation theory (CNT). In the proposed model and the LBM implementation, both location and time of nucleation are probabilistic (spatiotemporal stochastic dynamics), which may significantly impact the evolution of transport properties across time and length scales. More about probabilistic nucleation and how to implement it into pore-scale reactive transport models can be found in our previous works [8,10,12,22].

The D2Q9 lattice scheme was used in a 400×400 μm simulation domain representing a I) homogeneous nonreactive substrate and II) dual substrate system to model the surface nucleation and growth. All boundaries are subject to periodic boundary conditions. The domain is initially oversaturated with mineral A. An infinite source of a solution on top of the substrate was imposed. The first step in the LBM simulations is probabilistic nucleation, which is the necessary condition for growth or for the reaction to start $\{A_{(aq)} \rightleftarrows A_{(s)}\}$ [8,10,12]. As we previously showed [9,12], the nucleation and growth of the secondary phase on the initial substrate will create a new substrate in which nucleation will be more likely to occur. This is implemented into the model using weighted arithmetic averaging based on the surface area.

Four simulation scenarios for the dual substrate system are designed to evaluate the effect of relative interfacial free energy on the mineral distribution. The proportionality ratio of subdomains are as follows σ_2/σ_1 = [0.1, 0.5, 1, 1.6]. The interfacial free energy of the bottom-left and top-right parts of the domain is different from the rest.

2.5. Spatial randomness (entropy) evaluation

We computed Shannon's Entropy to quantify disorder and spatial randomness within the system. In 1948, Claude Shannon[47] introduced the classical definition of entropy in information theory for a random variable X with I possible categories. The entropy of a random variable is defined as the average level of information or probability inherent in the variable's possible outcomes. Given a random discrete variable X, with a likely domain of outcomes x_i $[x_1, x_2, \dots, x_n]$ and each with a probability of occurrence as $P(x_i)$ $[P(x_1), P(x_2), \dots, P(x_n)]$, the Shannon Entropy (E) of variable X is defined as:

$$E(x) = -\sum_{i=1}^{n} P(x_i) \log P(x_i) \quad (1)$$

Shannon's entropy measures the self-information of a variable. In other words, Shannon's entropy returns the expected value of a function, called information function, which measures the amount of information associated to each category x_i. The term information reflects the concepts of uncertainty or surprise. The information function $I(P(xi)) = log(1/P(xi))$ is a random variable, where $P(x_i)$ $[P(x_1), P(x_2), \dots, P(x_n)]$ is the univariate probability mass function (pmf) of X. Therefore, $E(X)$ measures the average amount of information provided by the realizations of X generated via the pmf $P(X)$.

A high entropy value means scarce information is available about the subsequent realization, which reflects on high uncertainty and heterogeneity of *X*. A low Shannon's entropy indicates a relatively inevitable outcome of the following observation, and as a result, uncertainty and heterogeneity of *X* are small. Based on the definition, the Entropy *E(X)* ranges in [0, log(i)], denoting that it is a nonnegative value with a maximum depending on the number of categories of *X*. The *E(X)* maximum value is achieved when *X* is uniformly distributed, while the minimum indicates the extreme case of certainty about the probabilistic outcome [48].

3. Results and Discussion

3.1. Carbonate synthesis column experiment on the basaltic glass substrate

Figure 2a shows a snapshot (image representing the state of a system at a particular point in time) and a schematic of the column reactor packed with calcite and basaltic glass during the flow-through of the CO_2-acidified seawater. Precipitation of calcium carbonate minerals at two temporal instances (7 and 21 days) at two different sections of the column is given (Fig. 2b). Figure 2b (top) depicts an enlarged body of white calcium carbonate precipitates on the background of dark basaltic glass after the experiments, along with the binary representation. Figure 2c presents high-resolution SEM (BSE and SE) and EDS analyses of the post-experiment samples, where the concentration of Ca^{2+} ion

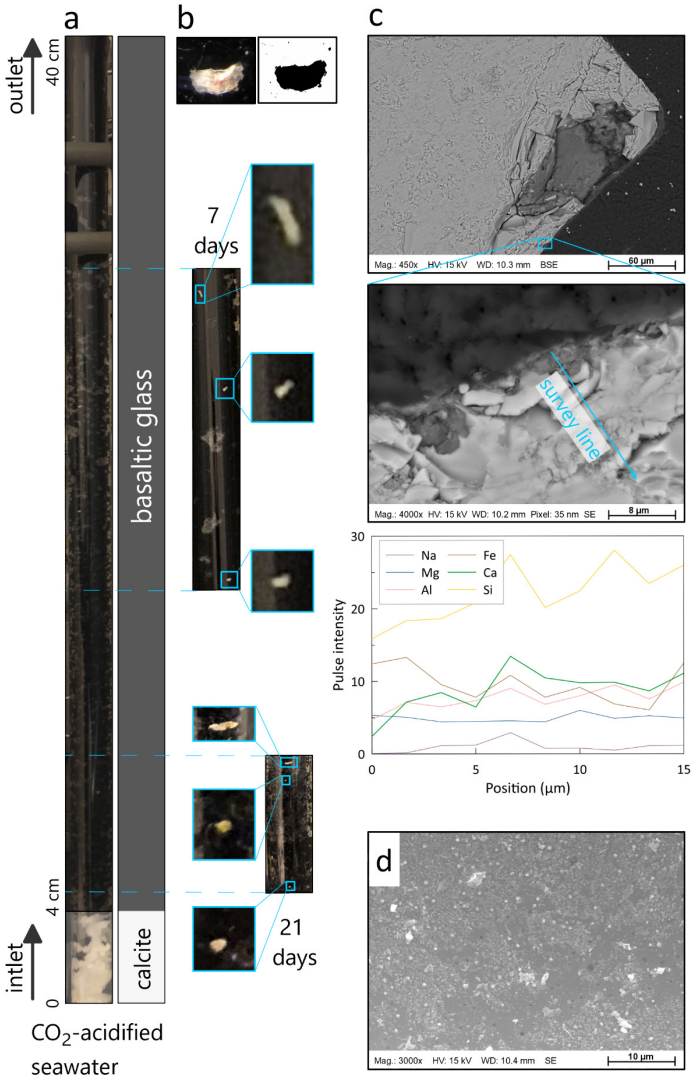

Fig. 2. (a) schematic of the column reactor packed with calcite and basaltic glass during the flow-through of the CO_2-acidified seawater. (b) calcium carbonate precipitation at two temporal instances (7 and 21 days) at two different sections of the column. (c) SEM (BSE and SE) and EDS analyses of a post-experiment sample, where the concentration of ions on the substrate surface is tracked and plotted over a survey line. (d) nucleation events and their early-stage non-crystalline shape on the surface of secondary substrates (previously precipitated carbonates).

(precipitated carbonates) is tracked and plotted over a survey line. Occurrences of nucleation events and their early-stage non-crystalline shape on the surface of secondary substrates (previously precipitated carbonates) are demonstrated in Figure 2d using the secondary electron imaging of the surface.

Continuous monitoring of this reactive transport experiment revealed that the precipitation location of the identified white patches is seemingly random along the entire column length (basalt section). Surprisingly, a larger number of accumulations occurred in the second half of the column compared to what was expected from the deterministic approach to occur at and close to the transition of calcite-basalt sections (Fig. 2b). Additionally, the observations illustrate that secondary precipitates formed as isolated pockets rather than dispersed aggregates in the entire column. These localized bodies of precipitates, their random spatial location of occurrence (and one might argue even temporal), and the fact that only a limited number but large crystal accumulations were formed suggest that overall precipitation reaction is controlled by nucleation rather than growth.

The acidity of the injected CO_2-charged seawater was measured routinely and was pH = 5.4-5.5 during the experimental period. Our aqueous geochemical calculations using PHREEQC (v3) suggest that after entering the column, the injected fluid first buffered to a pH of approximately 6 in equilibrium with calcite before the dissolution of basaltic glass further buffers the solution. The measured pH of outlet effluent solution showed a decreasing trend during the experimental time. It showed a decline in pH from 7.25 at the start to 6.58 at the end. The decline in pH over time could be associated with reduced basalt dissolution rates or increased precipitation of secondary carbonate phases with time. The PHREEQC simulations illustrate that carbonate minerals are stable, and the reacted aqueous solution becomes progressively more supersaturated (with respect to carbonates) as the solution advances through the column and reacts with the basalt substrate.

Figure 2c shows surface characterization at the boundary of one of the isolated calcium carbonate pockets, where the intensity of the pulse depicts the increase in calcium concentration on the surface. Figure 2d demonstrates that the affinity for nucleation and growth of secondary minerals is higher adjacent to or on top of the newly formed crystals than the original foreign substrate. The formation of the new nucleus and its consequent growth, creates a secondary substrate with a higher potential (probability) to form the following nuclei.

3.2. Surface precipitation microfluidic experiment on sandstone substrate

The energy-dispersive x-ray spectroscopy (EDS) elemental phase maps presented in Figure 3 provide insight into the solid formation on/in the natural multi-mineral heterogeneous substrate. It shows the preferential affinity for heterogeneous nucleation and subsequent growth on solid surfaces. In Figure 3, we present an SEM-EDS mosaic surface map with calcium carbonate crystals color-coded in green, a magnified section of the substrate, along with elemental phase maps of calcium (Ca) representing calcite, silica (Si) representing quartz, and aluminum (Al) and sodium (Na) representing feldspar grains.

Detailed investigation of high-resolution EDS-SEM surface maps indicates that at lower supersaturation ($\Omega = 15$), more selective nucleation and growth phenomena occur where spots with more favorable surface characteristics will be selected first. Visual randomness and entropy are apparent at higher Ω values ($\Omega = 130$). Even though a highly disordered system in Figure 3a is demonstrated where crystal growth is detectable almost everywhere, a detailed evaluation shows that several favored spots are still among the preferential locations. The favored sites for nucleation and subsequent growth are in the following order:

- carbonate cement, owing to the considerably lower interfacial free energy between the precipitating phase and carbonate cement compared to other grain-forming minerals
- rough substrate surfaces such as around the grain edges
- indentation and hollow surfaces such as holes

As shown in Figure 3a and the enlarged section, a pronounced accumulation of coalesced crystals is observable around the grain edges, where roughness and indentation surfaces are present. Experimental observations indicate that spatial locations characterized by surface roughness and irregularities host more mineral nucleation and subsequent crystal growth. Given similar physicochemical conditions, these preferential sites are formed due to differences in surface characteristics manifested in surface free energy and increased surface-interface potential to attract solid formation and growth.

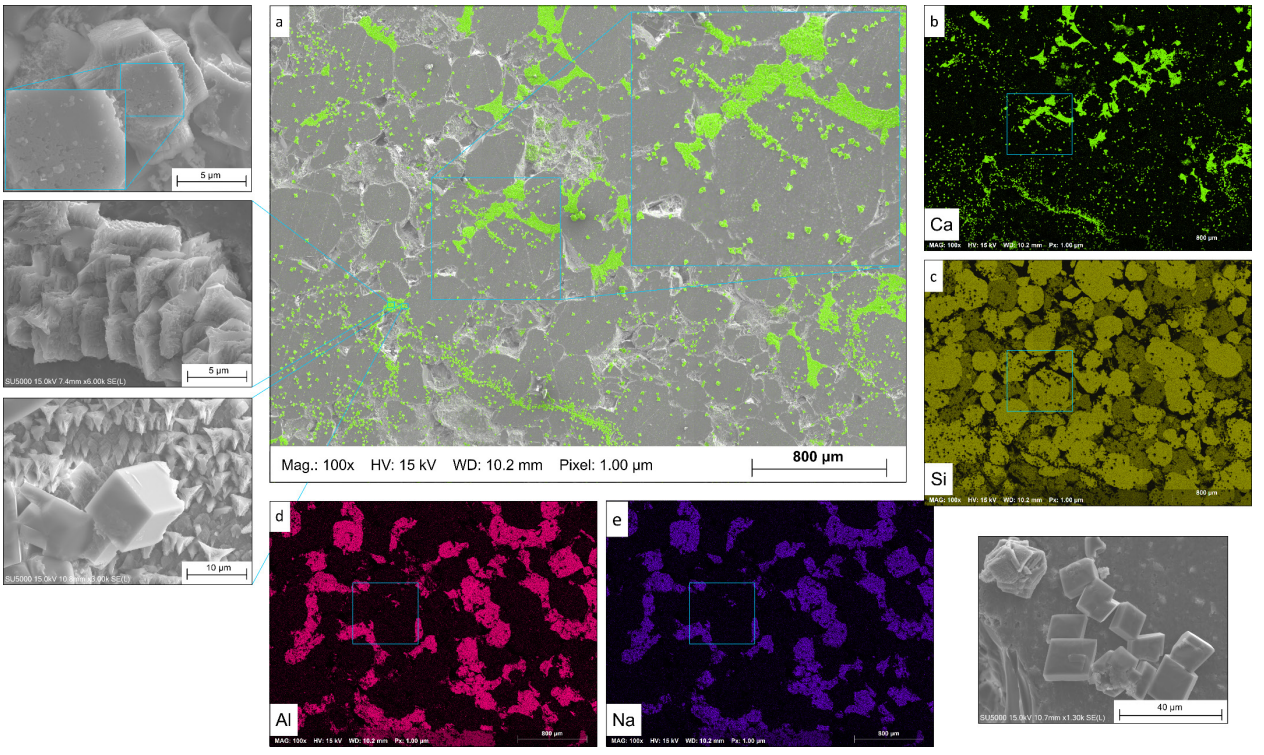

Fig. 3. EDS elemental phase maps of mineral formation on a heterogeneous sandstone substrate and preferential affinity for nucleation and growth. (a) SEM-EDS surface map with calcium carbonate crystals color-coded in green, a magnified section of the mosaic map, along with elemental phase maps of (b) calcium (Ca) representing calcite, (c) silica (Si) representing quartz, (d) aluminum (Al) and (e) sodium (Na) both representing feldspar grains. Additionally, nucleation (precipitation of primitive forms on crystal surfaces) on previously precipitated crystals, the preferential affinity to nucleate and grow on top and adjacent to secondary substrates is presented.

The SEM-EDS surface maps also demonstrate the impact of substrate composition on attracting nucleation events in heterogamous systems. In particular, in lower Ω values where the impact of preferences is pronounced, one can observe that certain mineral phases were the winning substrate in attracting more crystals than others. For instance, in Figure 3, the quartz grains were comparatively more favorable locations than feldspars (after the three favored spots listed above). Silica (Si) elemental phase map representing quartz (Fig. 3c) exhibits more solid accumulations (dark spots) compared to the aluminum (Al) and sodium (Na) representing feldspar grains.

Figure 3 also shows SE SEM micrographs of the substrate, where intergranular carbonate cement is present. As shown, there is almost no mineral growth on the sandstone substrate near the carbonate cement. The available solute concentration for nucleation and precipitation is attracted and consumed by the previous carbonate pockets (intergranular cement) owing to favorable interfacial free energy. The semi-conform morphology of accumulated crystals is notable, where individual crystals show a compact, coalesced, and overgrowth pattern. The co-presence of semi-conform precipitation patterns with coalesced crystalline geometries is also presented. The combination of these two latter cases can be exceptionally critical when describing the effects of crystallization-driven clogging in reactive transport models.

Additionally, in Figure 3, nucleation (precipitation of primitive forms on crystal surfaces) on previously precipitated crystals is presented. Furthermore, the preferential affinity to nucleate and grow on top and adjacent to secondary substrates contribute to increased coalescence between the crystals. The increased coalescence and interconnection, in turn, will attract increasingly more solutes towards the solid accumulation sites and, therefore, a faster growth rate compared to areas with isolated and dispersed crystals.

The image processing results of 27 experiments (3×3×3 sets of Ω-T-t) are presented in Figure 4, where the ratio of average covered surface area (%) divided by the number of precipitated crystals is given in the z-axis as a function of temperature and supersaturation. The size of the balls illustrates the average covered surface area. There are several observations on the impact of Ω-T-t on the dynamics of nucleation and growth, on which the reader is referred to our

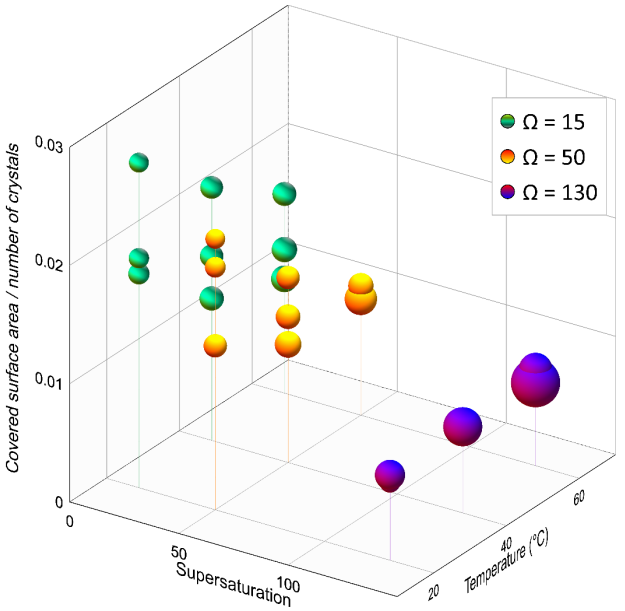

Fig. 4. ratio of average covered surface area (%) divided by the number of precipitated crystals (z-axis) as a function of temperature and supersaturation (x,y-axis). The size of the balls illustrates the average covered surface area.

previous work [9]. Here, we would like to highlight a rather important and novel observation. The area-to-count ratio in Figure 4 shows a decline with the increase in temperature and supersaturation. The impact of supersaturation is particularly pronounced. The lower area-to-count ratio at higher supersaturations can be associated with the higher number of nucleation events and growth sites at higher T-Ω, which did not coalesce and form interconnected pockets with comparable areal coverage. In other words, at lower Ω, a comparatively limited number of nuclei manage to crystallize and continue to form growth sites. These growth sites will then be able to attract available solute concentrations and produce more extensive pockets/patches of mineral accumulations. Therefore, a lower number of crystals and more extensive individual accumulations result in a higher area-to-count ratio at lower Ω (or T-Ω) conditions.

Additionally, the scatter in data points at a given condition (fixed T-Ω) also decreased at higher T-Ω values (Fig. 4). The more scatter in lower supersaturations (and lower T-Ω pairs) and the limited number of nucleation (and growth sites) suggest that randomness of the system (described by entropy) might be higher for lower supersaturations. In other words, based on Shannon's entropy definition, because scarce information is available about the status and range of potential realizations in low supersaturation (low T-Ω), a higher degree of uncertainty and heterogeneity in the stochastic dynamics of the system is expected.

3.3. Numerical simulation of dynamics of probabilistic nucleation and growth on the solid surface

The first step in LBM ADR simulations was to study the spatiotemporal evolution of crystal nucleation and growth on a homogenous substrate to limit the level of complexity of the observed stochastic dynamics. Figure 5 shows the effect of nucleation rate and reaction rate constant on the extent, distribution, and precipitation patterns. The ratio between the reaction and nucleation rates denoted as ϱ is:

$$\varrho = \frac{k_G}{R_N} = \frac{k_G}{\left(\frac{1}{\tau_N}\right)} \tag{2}$$

where, k_G [mol/m^2/s] is reaction rate constant, R_N [nuclei/m^2/s] is nucleation rate, and τ_N [m^2.s/ nuclei] is the induction time. Here, we present three simulation scenarios in which we kept ϱ constant and varied k_G (10^{-7} to 10^{-5}) and R_N (10^{-3} to 10^{-1}) over three orders of magnitude. In Figure 5, surface precipitation maps at four entropy levels (0.5 upward, 1, 0.5 downward, and when the substrate surface is fully covered), the corresponding time steps (evolution time) for each subfigure, and the overall Shannon's Entropy of the system from the initial state to entirely covered status are also presented.

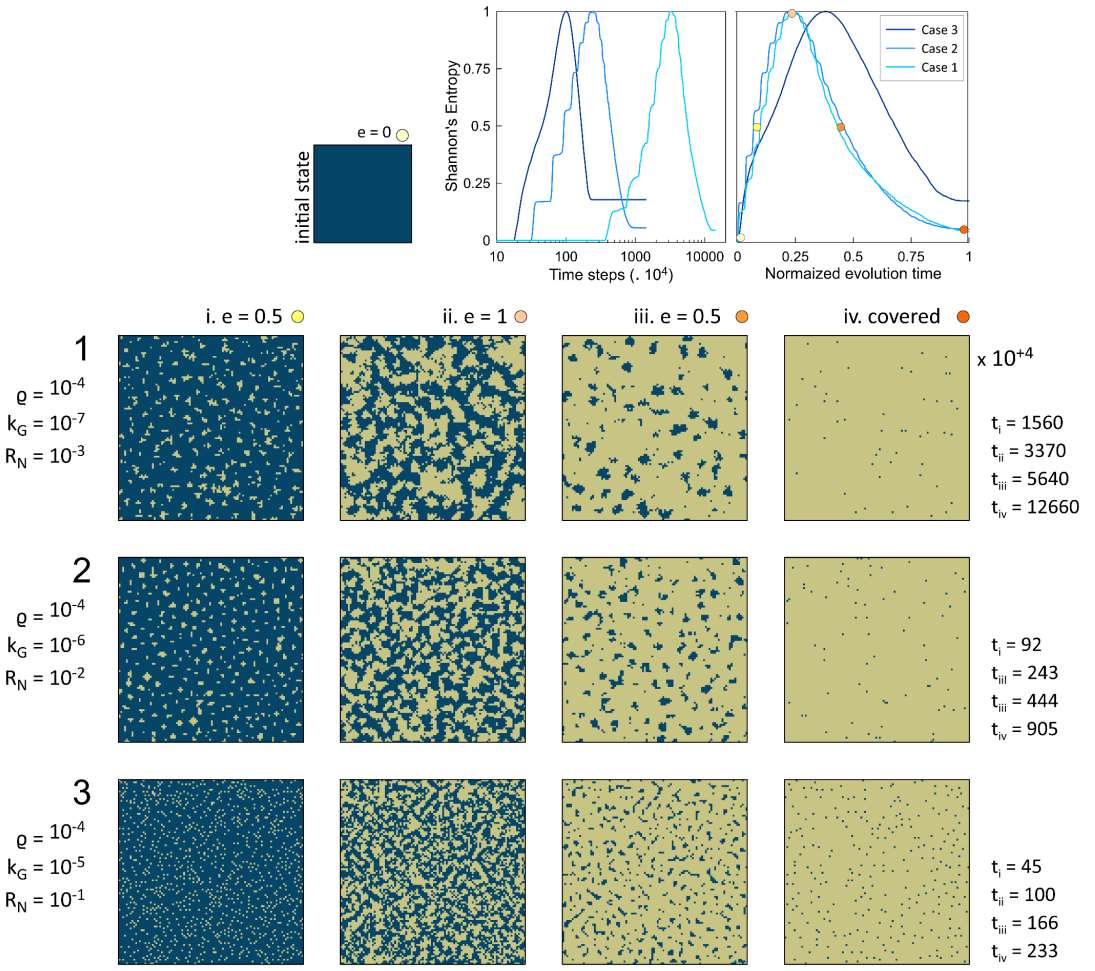

Fig. 5. surface precipitation maps of three LBM reactive transport simulation scenarios implementing probabilistic nucleation model are given over the entire evolution time of the system. For each scenario, the ratio between the reaction and nucleation rates (ϱ), reaction rate constant (k_G), nucleation rate (R_N), entropy level (e) together with the corresponding simulation time-steps ($\times 10^4$) are shown. The overall Shannon's Entropy of the system is also presented.

Detailed investigation of ϱ, k_G, and R_N parameters indicates reaction rate constant has primary control over the dynamics of crystal growth. k_G governs the interconnection and patchy accumulation of nuclei and consequently precipitated crystals leading to controlling the occupation of pore space during reactive transport processes. The pore occupancy and interconnection behavior make the underlying basis for defining a probabilistic clogging behavior. Besides precipitation time (or simulation time), the comparison scenarios 1-3 with similar ϱ suggest that lower k_G has led to (a) bigger crystal accumulations (cf. subfigures i with e = 0.5), (b) bigger inter-crystal pore volumes in early stages of solid formation (particularly in subplots i and ii), and (c) better surface coverage.

We computed entropy for each growth map per time step to assess the degree of randomness and probabilistic dynamics of nucleation and crystal growth. For the given simulation scenario, randomness and disorder measures show a Gauss-Laplace distribution. Entropy starts from a fully ordered system with no solid precipitation on the substrate. It increases as the solid phase emerges on the surface until randomness reaches the maximum value. Afterward, the overall disorder declines as more and more surface areas are covered, and eventually, entropy approaches zero towards an ordered state (fully covered). The entropy plots show a Gaussian bell function (normal distribution) with varying variance (σ^2). One also can argue that the q-Gaussian distribution might better represent the collective plots with varying q and β parameters. In scenario #3 in which fast precipitation is observed, the entropy curves show a right skewness with a rather abrupt increase in the degree of disorder since the first crystal. The faster

the growth, the narrower the standard deviation of the Gaussian bell. Plotted entropy in logarithmic scale distinguishes three evolution pathways based on their reaction rates. The normalized entropy curves demonstrate comparable q-Gaussian distributions for different simulation cases. The similarity is more noticeable for the slower simulation sets ($k_G = 10^{-6}$ and 10^{-7}).

In the probabilistic reactive LBM simulations, the randomness of the spatial distribution of crystals is ensured when we introduce probabilistic criteria for the location and number of nuclei. The growth on the primary and the secondary substrates is a function of the nucleation events. Figure 6 (a-h) represents eight realizations a given scenario (#2) at e = 0.85 entropy level (after approximately 180×10^4 time steps) to evaluate the randomness of spatial and temporal distributions. Following a probabilistic algorithm, the interplay between the reaction and nucleation governs the precipitation distributions. As Figure 6i shows, the overall evolution path described by the entropy of the realizations

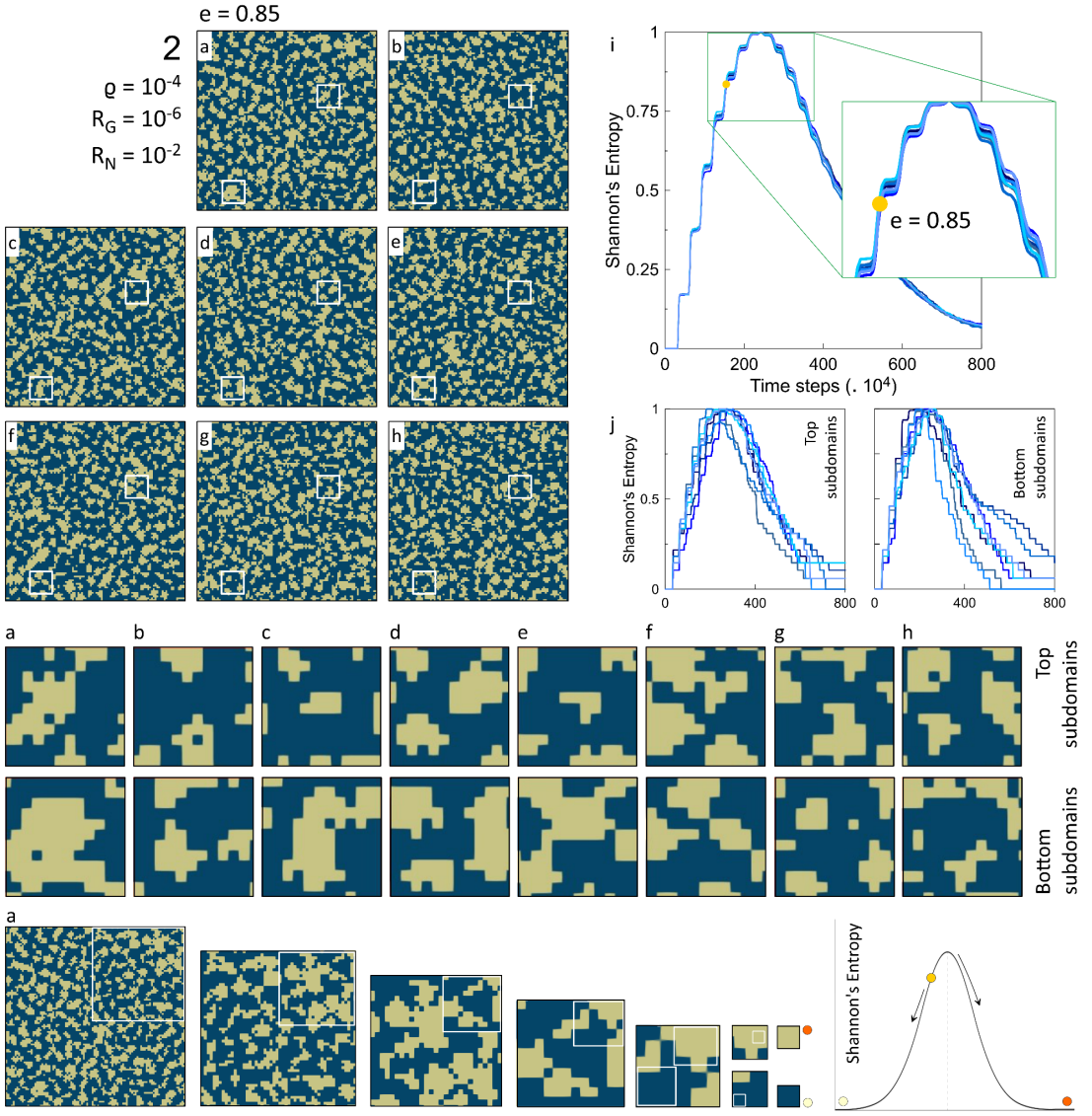

Fig. 6. (Left, a–h) eight different realizations of simulation scenario number 2 indicating stochastic amount and distribution of surface solid precipitation as implemented in probabilistic nucleation and crystal growth model. The white squares show the crystal accumulation status for two random REV subdomains. The subdomains (top and bottom squares) are enlarged for better comparison for each realization. (right, i) the computed Shannon entropy values for eight realizations during the entire simulation time ($\times 10^4$), describing the system's evolution pathways. (right, j) the computed Shannon entropy for subdomains (top and bottom squares) during the entire simulation time ($\times 10^4$). (bottom row) a sequence of surface precipitation maps where subdomains decrease in size (25% of areal size with respect to the previous domain).

is almost similar. Although, the pattern of surface precipitations, crystal locations, and their amount vary. The differences in these eight realizations is more evident when we consider smaller subdomains in each realization (white squares presented in the middle row of Figure 6).

Two subdomains are randomly selected for each realization, namely top and bottom subdomains. Each subdomain is enlarged to demonstrate the variations in smaller system sizes. For these two randomly picked locations, different precipitation amounts, different precipitation locations, and different growth patterns are observed. Moreover, the probabilistic control on crystal nucleation and precipitation within these two subdomains is better discernible compared to original domains (Fig. 6). Figure 6j shows the quantification of the spatial randomness of distributions. The degree of scatter and dissimilarity in evolution paths is markedly higher than the entropy of the original domain, particularly for the bottom subdomain's entropy plot. At a similar evolution time (approximately 180×10^4 time steps), the original realizations showed a 0.85 entropy level, while the disorder level in subdomains varies from 0.65 to 0.95 (Fig. 6j). It highlights that the size of the system and time matter for the entropy and thereby the randomness of the spatial distribution.

To further elucidate the impact of system spatial size (length scale) as we explained earlier with the conceptual framework (Fig. 1), a sequence of subdomains (25% of areal size with respect to the previous domain) is presented in the bottom row (Fig. 6) based on the subplot in Figure 6a. The potential changes in the entropy from e = 0.85 level are also depicted. The sequence of subdomains shows that with the decrease in the domain size, potential variations in the surface precipitation patterns may significantly increase. In extreme cases where the domain size approaches the grid cell size, two opposite potential outcomes might be equally probable: entirely reacted (fully covered) and entirely unreacted (spotless) substrate surface. This observation is also identifiable in the entropy plot, where a wide range of randomness values over the 2σ (twice the standard deviation) can be expected.

Our laboratory experiments showed several favorable locations for nucleation and growth (Figs. 2-3). To study the effect of these preferential nucleation sites on certain parts of the substrate and demonstrate the capability of our model for capturing it, we conducted the following simulations. Figure 7 shows the numerical results of modifying the interfacial free energy between the nucleating phase and the substrate. In Figure 7a-b, the bottom-left and top-right subdomains have smaller interfacial free energy than the rest of the domain (σ_2/σ_1 = 0.1 and 0.5). As a result, more mineral precipitation occurred in the areas with lower interfacial free energy. The lower the interfacial free energy (σ), the shorter the deterministic induction time (τ_N). The search for the probabilistic induction time (τ_P) takes place in the area expressed by a Gauss-Laplace probability density function with the τ_N as the average value ($\mu = \tau_N$) [10,12]. As a result, the probability of a nucleation event is higher in the areas with shorter induction times (here, due to lower interfacial free energy). Nucleation is necessary for growth, so a combination of more nucleation events and earlier nucleation events will result in more accumulation of mineral precipitation in favorable areas.

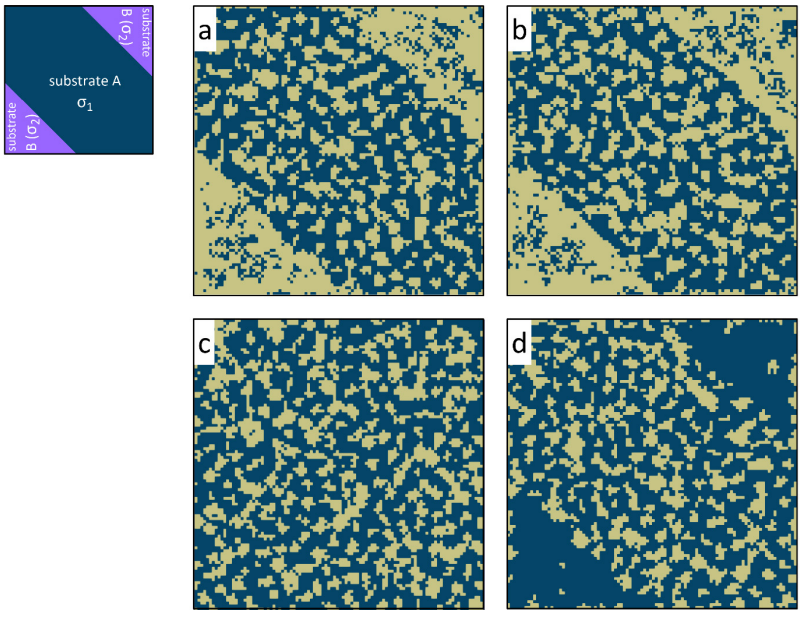

Fig. 7. sensitivity analysis of the interfacial free energy between the nucleating phase and the substrate surface in a dual-medium solid. The proportionality ratio of subdomains are as follows σ2/σ1 = (a) 0.1, (b) 0.5, (c) 1, and (d) 1.6.

In Figure 7c, the secondary mineral precipitates are evenly distributed over the entire domain with similar growth patterns owing to the same σ (no favorable nucleation region exists as $\sigma_2/\sigma_1 = 1$). On the other hand, in Figure 7d, where the bottom-left and top-right portions have larger interfacial free energy than the rest of the domain ($\sigma_2/\sigma_1 = 1.6$), the mineral accumulations are concentrated in the inner part of the domain. Because of the probabilistic nature, however, nucleation events still occurred at high interfacial free energy regions. A comparison between simulation scenarios (a) and (d) in Figure 7 indicates how probabilistic nucleation and growth may control the evolution of the porous medium. In these two scenarios, the differences in interfacial free energy of subdomains (corner and inner regions) led to different nucleation locations, precipitation amount, and growth patterns.

4. Concluding remarks

The current study presents an experimental and numerical investigation of surface mineral nucleation, precipitation, and growth. The aim was to provide pore-scale observations and insights into the stochastic dynamics of the phenomena via the implementation of the new model for probabilistic nucleation and growth. We delineated nucleation as the first step in the precipitation and growth chain of events. The results indicated the probabilistic nature of the process, which is affected by the physiochemistry of the aqueous phase and governed by fluid-solid surface interactions. The research outcomes highlighted that it is crucial to consider surface properties, preferential locations, and nucleation and growth on the previously precipitated crystal (secondary substrate). We underscore the importance of theoretical reactive transport models considering nucleation and its probabilistic characteristics before crystal formation. Laboratory results and LBM simulations indicated that supersaturation and reaction rate strongly control the mineral nucleation and crystal growth, resulting in changes in the morphology of the newly precipitated solid phase. Altering pore network characteristics, including connectivity, tortuosity, and architecture, and changes in surface roughness induced by solid formation, can render numerous variations in absolute and effective permeability. Such reality may not be captured by Kozeny-Carman, Hagen–Poiseuille, Fair-Hatch type or power-law porosity-permeability relationships, which are implemented in almost all available reactive transport packages.

Acknowledgments

This publication has been produced with support from the project "solid and salt precipitation kinetics during CO_2 injection into reservoir" (SaltPreCO_2), funded by the EEA and Norway Grants, Norwegian Financial Mechanism 2014-2021, (UMO-2019/34/H/ST10/00564) through the GRIEG Program, operated by the Polish National Science Centre (NCN) in cooperation with the Research Council of Norway (Norges Forskningsråd). The high-performance computing was carried out on the Norwegian Research and Education Cloud (NREC), provided by the University of Bergen and the University of Oslo (UiO). MN express gratitude towards the UiO:Energy for the support via the International Mobility and Collaboration Grant and the Faculty of Mathematics and Natural Sciences (UiO) for the Kristine Bonnevie Grant.

References

1. Deng, H.; Poonoosamy, J.; Molins, S. A reactive transport modeling perspective on the dynamics of interface-coupled dissolution-precipitation. *Appl. Geochemistry* **2022**, *137*, 105207, doi:https://doi.org/10.1016/j.apgeochem.2022.105207.
2. Renard, F.; Røyne, A.; Putnis, C. V Timescales of interface-coupled dissolution-precipitation reactions on carbonates. *Geosci. Front.* **2019**, *10*, 17–27, doi:https://doi.org/10.1016/j.gsf.2018.02.013.
3. Rajyaguru, A.; Seigneur, N.; Bildstein, O.; Savoye, S.; Wittebroodt, C.; Hôpital, E.L.; Detilleux, V.; Arnoux, P.; Lagneau, V. Barite and gypsum precipitation in chalk: A numerical simulation approach revealing the coupled impact of physical and chemical heterogeneities in porous media. *Chem. Geol.* **2022**, 121069, doi:https://doi.org/10.1016/j.chemgeo.2022.121069.
4. Ruiz-Agudo, E.; Putnis, C. V; Putnis, A. Coupled dissolution and precipitation at mineral–fluid interfaces. *Chem. Geol.* **2014**, *383*, 132–146, doi:https://doi.org/10.1016/j.chemgeo.2014.06.007.
5. Nooraiepour, M. Rock properties and sealing efficiency in fne-grained siliciclastic caprocks — Implications for CCS and petroleum industry, University of Oslo: Oslo, Norway, 2018, Vol. PhD.
6. Poonoosamy, J.; Lu, R.; Lönartz, M.I.; Deissmann, G.; Bosbach, D.; Yang, Y. A Lab on a Chip Experiment for Upscaling

Diffusivity of Evolving Porous Media. *Energies* 2022, *15*.
7. Nooraiepour, M.; Fazeli, H.; Miri, R.; Hellevang, H. Effect of CO2 Phase States and Flow Rate on Salt Precipitation in Shale Caprocks - A Microfluidic Study. *Environ. Sci. Technol.* **2018**, *52*, 6050–6060, doi:10.1021/acs.est.8b00251.
8. Fazeli, H.; Masoudi, M.; Patel, R.A.; Aagaard, P.; Hellevang, H. Pore-Scale Modeling of Nucleation and Growth in Porous Media. *ACS Earth Sp. Chem.* **2020**, *4*, 249–260, doi:10.1021/acsearthspacechem.9b00290.
9. Nooraiepour, M.; Masoudi, M.; Shokri, N.; Hellevang, H. Probabilistic Nucleation and Crystal Growth in Porous Medium: New Insights from Calcium Carbonate Precipitation on Primary and Secondary Substrates. *ACS Omega* **2021**, *6*, 28072–28083, doi:10.1021/acsomega.1c04147.
10. Masoudi, M.; Fazeli, H.; Miri, R.; Hellevang, H. Pore scale modeling and evaluation of clogging behavior of salt crystal aggregates in CO2-rich phase during carbon storage. *Int. J. Greenh. Gas Control* **2021**, *111*, 103475, doi:https://doi.org/10.1016/j.ijggc.2021.103475.
11. Fazeli, H.; Nooraiepour, M.; Hellevang, H. Microfluidic Study of Fracture Dissolution in Carbonate-Rich Caprocks Subjected to CO2-Charged Brine. *Ind. Eng. Chem. Res.* **2020**, *59*, doi:10.1021/acs.iecr.9b06048.
12. Nooraiepour, M.; Masoudi, M.; Hellevang, H. Probabilistic nucleation governs time, amount, and location of mineral precipitation and geometry evolution in the porous medium. *Sci. Rep.* **2021**, *11*, doi:10.1038/s41598-021-95237-7.
13. Seigneur, N.; Mayer, K.U.; Steefel, C.I. Reactive Transport in Evolving Porous Media. *Rev. Mineral. Geochemistry* **2019**, *85*, 197–238, doi:10.2138/rmg.2019.85.7.
14. An, S.; Hasan, S.; Erfani, H.; Babaei, M.; Niasar, V. Unravelling Effects of the Pore-Size Correlation Length on the Two-Phase Flow and Solute Transport Properties: GPU-based Pore-Network Modeling. *Water Resour. Res.* **2020**, *56*, e2020WR027403, doi:https://doi.org/10.1029/2020WR027403.
15. An, S.; Erfani, H.; Hellevang, H.; Niasar, V. Lattice-Boltzmann simulation of dissolution of carbonate rock during CO2-saturated brine injection. *Chem. Eng. J.* **2021**, *408*, 127235, doi:https://doi.org/10.1016/j.cej.2020.127235.
16. Beckingham, L.E. Evaluation of Macroscopic Porosity-Permeability Relationships in Heterogeneous Mineral Dissolution and Precipitation Scenarios. *Water Resour. Res.* **2017**, *53*, 10217–10230, doi:https://doi.org/10.1002/2017WR021306.
17. Shokri-Kuehni, S.M.S.; Bergstad, M.; Sahimi, M.; Webb, C.; Shokri, N. Iodine k-edge dual energy imaging reveals the influence of particle size distribution on solute transport in drying porous media. *Sci. Rep.* **2018**, *8*, 10731, doi:10.1038/s41598-018-29115-0.
18. Shahidzadeh-Bonn, N.; Desarnaud, J.; Bertrand, F.; Chateau, X.; Bonn, D. Damage in porous media due to salt crystallization. *Phys. Rev. E* **2010**, *81*, 66110, doi:10.1103/PhysRevE.81.066110.
19. Nooraiepour, M.; Fazeli, H.; Miri, R.; Hellevang, H. Salt Precipitation during Injection of CO2 into Saline Aquifers: Lab-on-Chip Experiments on Glass and Geomaterial Microfluidic Specimens. *SSRN* **2019**, doi:10.2139/ssrn.3365553.
20. Molins, S.; Trebotich, D.; Miller, G.H.; Steefel, C.I. Mineralogical and transport controls on the evolution of porous media texture using direct numerical simulation. *Water Resour. Res.* **2017**, *53*, 3645–3661, doi:10.1002/2016WR020323.
21. Steefel, C.I.; Molins, S.; Trebotich, D. Pore Scale Processes Associated with Subsurface CO2 Injection and Sequestration. *Rev. Mineral. Geochemistry* **2013**, *77*, 259–303, doi:10.2138/rmg.2013.77.8.
22. Masoudi, M.; Nooraiepour, M.; Hellevang, H. The Effect of Preferential Nucleation Sites on the Distribution of Secondary Mineral Precipitates. In Proceedings of the 83rd EAGE Annual Conference & Exhibition; European Association of Geoscientists & Engineers: Madrid, Spain, 2022; Vol. 2022, pp. 1–5.
23. Deng, H.; Spycher, N. Modeling Reactive Transport Processes in Fractures. *Rev. Mineral. Geochemistry* **2019**, *85*, 49–74, doi:10.2138/rmg.2019.85.3.
24. Soulaine, C.; Roman, S.; Kovscek, A.; Tchelepi, H.A. Mineral dissolution and wormholing from a pore-scale perspective. *J. Fluid Mech.* **2017**, *827*, 457–483, doi:10.1017/jfm.2017.499.
25. Menke, H.P.; Reynolds, C.A.; Andrew, M.G.; Pereira Nunes, J.P.; Bijeljic, B.; Blunt, M.J. 4D multi-scale imaging of reactive flow in carbonates: Assessing the impact of heterogeneity on dissolution regimes using streamlines at multiple length scales. *Chem. Geol.* **2018**, *481*, 27–37, doi:https://doi.org/10.1016/j.chemgeo.2018.01.016.
26. Prasianakis, N.I.; Curti, E.; Kosakowski, G.; Poonoosamy, J.; Churakov, S. V Deciphering pore-level precipitation mechanisms. *Sci. Rep.* **2017**, *7*, 13765, doi:10.1038/s41598-017-14142-0.
27. Poonoosamy, J.; Soulaine, C.; Burmeister, A.; Deissmann, G.; Bosbach, D.; Roman, S. Microfluidic flow-through reactor and 3D Raman imaging for in situ assessment of mineral reactivity in porous and fractured porous media. *Lab Chip* **2020**, *20*, 2562–2571.
28. Hellevang, H.; Wolff-Boenisch, D.; Nooraiepour, M. Kinetic control on the distribution of secondary precipitates during

CO2-basalt interactions. In Proceedings of the E3S Web of Conferences; 2019; Vol. 98.
29. Hellevang, H.; Pham, V.T.H.; Aagaard, P. Kinetic modelling of CO2–water–rock interactions. *Int. J. Greenh. Gas Control* **2013**, *15*, 3–15, doi:https://doi.org/10.1016/j.ijggc.2013.01.027.
30. Noiriel, C.; Steefel, C.I.; Yang, L.; Ajo-Franklin, J. Upscaling calcium carbonate precipitation rates from pore to continuum scale. *Chem. Geol.* **2012**, *318*, 60–74.
31. Fazeli, H.; Patel, R.A.; Ellis, B.R.; Hellevang, H. Three-Dimensional Pore-Scale Modeling of Fracture Evolution in Heterogeneous Carbonate Caprock Subjected to CO2-Enriched Brine. *Environ. Sci. Technol.* **2019**, *53*, 4630–4639, doi:10.1021/acs.est.8b05653.
32. Jambhekar, V.A.; Helmig, R.; Schröder, N.; Shokri, N. Free-Flow–Porous-Media Coupling for Evaporation-Driven Transport and Precipitation of Salt in Soil. *Transp. Porous Media* **2015**, *110*, 251–280, doi:10.1007/s11242-015-0516-7.
33. Noiriel, C.; Soulaine, C. Pore-Scale Imaging and Modelling of Reactive Flow in Evolving Porous Media: Tracking the Dynamics of the Fluid–Rock Interface. *Transp. Porous Media* **2021**, *140*, 181–213, doi:10.1007/s11242-021-01613-2.
34. Molins, S.; Knabner, P. Multiscale Approaches in Reactive Transport Modeling. *Rev. Mineral. Geochemistry* **2019**, *85*, 27–48, doi:10.2138/rmg.2019.85.2.
35. De Yoreo, J.J.; Vekilov, P.G. Principles of crystal nucleation and growth. *Biomineralization* **2003**, *54*, 57–93.
36. Dimitrov, I.L.; Hodzhaoglu, F. V; Koleva, D.P. Probabilistic approach to lysozyme crystal nucleation kinetics. *J. Biol. Phys.* **2015**, *41*, 327–338, doi:10.1007/s10867-015-9381-4.
37. Sosso, G.C.; Chen, J.; Cox, S.J.; Fitzner, M.; Pedevilla, P.; Zen, A.; Michaelides, A. Crystal Nucleation in Liquids: Open Questions and Future Challenges in Molecular Dynamics Simulations. *Chem. Rev.* **2016**, *116*, 7078–7116, doi:10.1021/acs.chemrev.5b00744.
38. Li, Q.; Jun, Y.-S. The apparent activation energy and pre-exponential kinetic factor for heterogeneous calcium carbonate nucleation on quartz. *Commun. Chem.* **2018**, *1*, 56, doi:10.1038/s42004-018-0056-5.
39. Yang, F.; Yuan, K.; Stack, A.G.; Starchenko, V. Numerical Study of Mineral Nucleation and Growth on a Substrate. *ACS Earth Sp. Chem.* **2022**, *6*, 1655–1665, doi:10.1021/acsearthspacechem.1c00376.
40. Starchenko, V. Pore-Scale Modeling of Mineral Growth and Nucleation in Reactive Flow . *Front. Water* 2022, *3*.
41. Gislason, S.R.; Oelkers, E.H. Mechanism, rates, and consequences of basaltic glass dissolution: II. An experimental study of the dissolution rates of basaltic glass as a function of pH and temperature. *Geochim. Cosmochim. Acta* **2003**, *67*, 3817–3832, doi:https://doi.org/10.1016/S0016-7037(03)00176-5.
42. Wolff-Boenisch, D.; Gislason, S.R.; Oelkers, E.H.; Putnis, C. V The dissolution rates of natural glasses as a function of their composition at pH 4 and 10.6, and temperatures from 25 to 74°C. *Geochim. Cosmochim. Acta* **2004**, *68*, 4843–4858, doi:https://doi.org/10.1016/j.gca.2004.05.027.
43. Moghadam, J.N.; Nooraiepour, M.; Hellevang, H.; Mondol, N.H.; Aagaard, P. Relative permeability and residual gaseous CO2 saturation in the Jurassic Brentskardhaugen Bed sandstones, Wilhelmøya Subgroup, western central Spitsbergen, Svalbard. *Nor. J. Geol.* **2019**, *99*, 1–12, doi:10.17850/njg005.
44. Nooraiepour, M.; Bohloli, B.; Park, J.; Sauvin, G.; Skurtveit, E.; Mondol, N.H.H. Effect of brine-CO2 fracture flow on velocity and electrical resistivity of naturally fractured tight sandstones. *Geophysics* **2018**, *83*, WA37–WA48, doi:10.1190/GEO2017-0077.1.
45. Parkhurst, D.L.; Appelo, C.A.J. *Description of input and examples for PHREEQC version 3: a computer program for speciation, batch-reaction, one-dimensional transport, and inverse geochemical calculations*; Reston, VA, 2013;
46. Schindelin, J.; Arganda-Carreras, I.; Frise, E.; Kaynig, V.; Longair, M.; Pietzsch, T.; Preibisch, S.; Rueden, C.; Saalfeld, S.; Schmid, B.; et al. Fiji: an open-source platform for biological-image analysis. *Nat. Methods* **2012**, *9*, 676–682, doi:10.1038/nmeth.2019.
47. Shannon, C.E. A mathematical theory of communication. *Bell Syst. Tech. J.* **1948**, *27*, 379–423, doi:10.1002/j.1538-7305.1948.tb01338.x.
48. Altieri, L.; Cocchi, D.; Roli, G. A new approach to spatial entropy measures. *Environ. Ecol. Stat.* **2018**, *25*, 95–110, doi:10.1007/s10651-017-0383-1.